molecules

MDPI

Article

Synthesis of samarium oxysulfate $Sm_2O_2SO_4$ in the high-temperature oxidation reaction and its structural, thermal and luminescent properties

Yu.G. Denisenko[1], E.I. Sal'nikova[2,3], S.A. Basova[2], M.S. Molokeev[4,5,6], A.S. Krylov[7], A.S. Aleksandrovsky[8,9], A.S. Oreshonkov[5,7], V.V. Atuchin[10,11,12,*], S.S. Volkova[13], N.A. Khritokhin[2] and O.V. Andreev[2,14]

[1] Department of General and Special Chemistry, Industrial University of Tyumen, Tyumen 625000, Russia; yu.g.denisenko@gmail.com
[2] Institute of Chemistry, Tyumen State University, Tyumen 625003, Russia; elenasalnikova213@gmail.com (E.I.S.); basovasofia@yandex.ru (S.A.B.); kna@utmn.ru (N.A.K.); o.v.andreev@utmn.ru (O.V.A.)
[3] Department of General Chemistry, Northen Trans-Ural Agricultural University, Tyumen, 625003, Russia
[4] Laboratory of Crystal Physics, Kirensky Institute of Physics, Federal Research Center KSC SB RAS, Krasnoyarsk 660036, Russia; msmolokeev@mail.ru
[5] Siberian Federal University, Krasnoyarsk 660041, Russia; oreshonkov@iph.krasn.ru
[6] Department of Physics, Far Eastern State Transport University, Khabarovsk 680021, Russia
[7] Laboratory of Molecular Spectroscopy, Kirensky Institute of Physics Federal Research Center KSC SB RAS, Krasnoyarsk 660036, Russia; shusy@iph.krasn.ru
[8] Laboratory of Coherent Optics, Kirensky Institute of Physics Federal Research Center KSC SB RAS, Krasnoyarsk 660036, Russia; aleksandrovsky@kirensky.ru
[9] Institute of Nanotechnology, Spectroscopy and Quantum Chemistry, Siberian Federal University, Krasnoyarsk 660041, Russia
[10] Laboratory of Optical Materials and Structures, Institute of Semiconductor Physics, SB RAS, Novosibirsk 630090, Russia
[11] Functional Electronics Laboratory, Tomsk State University, Tomsk 634050, Russia
[12] Research and Development Department, Kemerovo State University, Kemerovo 650000, Russia
[13] Research Resource Center "Natural Resource Management and Physico-Chemical Research", Tyumen State University, Tyumen 625003, Russia; svolkova2008@mail.ru
[14] Institute of Solid State Chemistry, UB RAS, Ekaterinburg, 620137, Russia
* Correspondence: atuchin@isp.nsc.ru; Tel.: (optional; include country code; if there are multiple corresponding authors, add author initials) +xx-xxxx-xxx-xxxx

Received: date; Accepted: date; Published: date

Abstract: The oxidation process of samariumoxysulfide was studied in the temperature range of 500-1000ºC. Our DTA investigation allowed establishing the main thermodynamic (ΔH^{o}_{exp} = –654.6 kJ/mol) and kinetic characteristics of the process (E_a = 244 kJ/mol, A = $2 \cdot 10^{10}$).The enthalpy value of samarium oxysulfate ($\Delta H^{o}f$ ($Sm_2O_2SO_{4(monocl)}$) = –2294.0 kJ/mol) formation was calculated. The calculated process enthalpy value coincides with the value determined in the experiment. It was established that samarium oxysulfate crystallizes in the monoclinic symmetry class and its crystal structure belongs to space group C2/*c* with unit cell parameters *a* = 13.7442 (2), *b* = 4.20178 (4) and *c* = 8.16711 (8)Å, β = 107.224 (1)°, *V* = 450.498 (9)Å^3, *Z* = 4. The main elements of the crystalline structure are obtained and the cation coordination environment is analyzed in detail. Vibrational spectroscopy methods confirmed the structural model adequacy. The $Sm_2O_2SO_4$luminescence spectra exhibit three main bands easily assignable to the transitions from $^4G_{5/2}$ state to $^6H_{5/2}$, $^6H_{7/2}$, and $^6H_{9/2}$ multiplets.

Keywords: samarium; oxysulfate; structure; luminescence; thermochemistry

1. Introduction

The compounds of rare-earth elements (REE) with tetrahedral anions, possessing a set of rather valuable properties, have attracted the attention of researchers for recent years. In particular, rare earth oxysulfates are used as precursors for the production of REE_2O_2S compounds [1-3]. The materials containing oxysulfates are of practical importance as phosphorescent material components and they can be used in X-ray computed tomography and the detection of radioactive radiation [4-7]. The structural and chemical properties of $REE_2O_2SO_4$ oxysulfates make it possible to consider them as promising materials for the chemical adsorption and storage of gaseous oxygen [8–11]. Commonly, oxysulfates are formed upon the decomposition of REE compounds containing, at least, one sulfate group: $REE_2(SO_4)_3$ [12-15], $REE_2(OH)_4SO_4$ [16, 17]. Oxysulfates can also be obtained by the decomposition of organic sulfonates of various structures [18]. A direct synthesis method consists of the temperature treatment of oxides in the atmosphere of sulfur oxide (IV) and oxygen [19].

Usually, lanthanide ions, due to forbidden electronic *f-f* transitions, are doping components in different materials and, in this form, they exhibit the properties of phosphors [20-25]. In many cases, however, the unobvious crystallographic positions of doping ions in such compounds induce certain difficulties in the observation of such materials [26, 27]. Thermal decomposition methods are a convenient tool for producing compounds and materials with desired properties. As it is known from the reported results, the initial material granules, under certain conditions, are able to maintain the original shape and size in the thermal decomposition process [28-30]. At the same time, the compounds with the stoichiometric lanthanide ion content attract attention in order to find efficient luminescent materials with low concentration quenching and to investigate specific mechanisms of luminescence quenching in them. [31-40]. At the same time, the consideration of lanthanide-containing materials can not be restricted only by their luminescent properties. The possibility of using lanthanide compounds with simple and complex anions as paramagnetic, catalytic, scintillation and solid oxide-fuel materials are being increasingly discussed [41-46]. The present study is aimed at the samarium oxysulfate synthesis in the high-temperature oxidative process and exploration of their structural, thermal and spectroscopic properties.

2. Materials and Methods

2.1. Synthesis methods

Samarium oxysulfide was obtained by the reduction of samarium sulfate $Sm_2(SO_4)_3$ (99.9%, Merck Ltd., Germany) in the hydrogen atmosphere at the temperature of 700°C. The installation scheme for carrying out the high-temperature recovery processes is shown in Figure S1. High purity hydrogen was obtained by the electrolytic method in a SPECTR - 6M hydrogen generator. The temperature control and regulation were carried out using a microprocessor controller. The temperature measurement in the reaction zone was provided by a chromel-alumel thermocouple. A weighed amount of dry $Sm_2(SO_4)_3$ was placed in a quartz reactor and it was purged with hydrogen from the generator for 30 min at the rate of 6 l/h. After that, the reactor was placed in a heated vertical furnace and kept for 5 h. After the completion of recovery process, the reactor was removed from the furnace and cooled to room temperature. The process proceeding during the recovery is described by the equation:

$$Sm_2(SO_4)_3 + 12H_2 \rightarrow Sm_2O_2S + 2H_2S\uparrow + 10H_2O\uparrow \quad (5)$$

To study the samarium oxysulfide oxidation with air oxygen, 0.5 g Sm_2O_2S sample was uniformly distributed as a thin layer over a ceramic boat bottom with the area of 3×5 cm^2. In order to prevent the tight layer formation during the oxidation process, all samarium oxysulfide samples were crushed in an agate mortar with acetone addition. After the filling, the ceramic boat was placed in a horizontal furnace heated to the required temperature and the processing was carried out in a continuous air flow. After the required time, the boat was removed from the oven and cooled to room temperature in a desiccator with the silica gel to avoid surface hydration. A study of the phase

composition of obtained oxidized sample was carried out by the X-ray diffraction method. The isothermal oxidation experiments were carried out at the temperatures of 500, 600, 700, 800, 900 and 1000ºC. The total time of the oxidation process at each temperature did not exceed 10 h.

3.2. Methods of physico-chemical analysis

The thermal analysis in the synthetic air (80% Ar-20% O_2) flow was carried out on a Simultaneous Thermal Analysis (STA) equipment 499 F5 Jupiter NETZSCH (Germany). The powder samples were inserted into alumina crucibles. The heating rate was 3°C/min. For the enthalpy determination, the equipment was calibrated with the use of standard metal substances, such as In, Sn, Bi, Zn, Al, Ag, Au and Ni. The heat effect peaks were determined with the package «Proteus 6 2012». The peak temperature and area in parallel experiments were reproduced at an inaccuracy lower than 3%. The kinetic parameters determination was based on Kissinger formula [47] in the linearized form:

$$\frac{1}{T} = \frac{R}{E} ln \frac{AR}{E} - \frac{1}{E} Rln \frac{b}{T^2}$$

where T is the temperature with a maximum reaction rate; b - heating rate; E - activation energy and A - preexponential factor. The representative examples of using the formula in topochemical processes can be found elsewhere [48-50].

To determine the phase composition of the samples at various oxidation stages, we used a BRUKER D2 PHASER X-ray diffractometer with a linear detector LYNXEYE (CuKα radiation, Ni-filter). The crystal structure was refined using the Rietveld method in the TOPAS 4.2 program [51]. The powder diffraction data of $Sm_2O_2SO_4$ for Rietveld analysis were collected at room temperature with a Bruker D8 ADVANCE powder diffractometer (Cu-Kα radiation) equipped with a linear detector VANTEC. The step size of 2θ was 0.016° and the counting time was 5 s per step. The particle morphology analysis was carried out on an electron microscope JEOL JSM-6510LV. The X-ray energy-dispersive analyzer was used to register the X-ray signal at recording the element spectrum in the selected regions of sample surface. The possible element content determination inaccuracy in the chemical composition determination by this method was equal to ±0.2%. The Fourier-transform infrared spectroscopy (FTIR) analysis was carried out with the use of Fourier Transform Infrared Spectrometer FSM 1201. The sample for the investigation was prepared in the tablet shape with the addition of annealed KBr. The Raman scattering spectra of $Sm_2O_2SO_4$ were collected in backscattering geometry, using a triple monochromator Horiba Jobin Yvon T64000 Raman spectrometer operating in subtractive mode. The spectral resolution for the recorded Stokes side Raman spectra was about 1 cm^{-1} (this resolution was achieved by using gratings with 1800 grooves mm^{-1} and 100 micrometer slits). Single-mode krypton 647.1 nm of Lexel Kr^+ laser of 3 mW on the sample was used as an excitation light source. The luminescence spectra at room temperature were recorded using a Horiba-Jobin-Yvon T64000 spectrometer and GaN laser diode with the central wavelength 410 nm. Spectral resolution of the measurement channel of the spectrometer was 2.7 cm^{-1}.

3. Results and Discussion

3.1. Dynamic oxidation of Sm_2O_2S and thermal stability of $Sm_2O_2SO_4$

According to the differential thermal analysis (Fig. 1.a), the samarium oxysulfide oxidation begins at the temperature of 550°C, proceeds in one stage and ends at 775°C. The mass gain corresponds to the samarium oxysulfate ($Sm_2O_2SO_4$) formation. The process is described by the reaction equation:

$$Sm_2O_2S + 2O_2 \rightarrow Sm_2O_2SO_4 \quad (1)$$

The resulting samarium oxysulfate is stable up to 1100°C, and, then, it decomposes in one stage with the Sm_2O_3formation. The process can be described by the equation:

$$Sm_2O_2SO_4 \rightarrow Sm_2O_3 + SO_2 + {}^1/_2O_2 \quad (2)$$

139 The certain enthalpies of the two reactions allow us to write thermochemical equations:

$$Sm_2O_2S_{(trig)} + 2O_{2(gas)} \rightarrow Sm_2O_2SO_{4(monocl)};\ \Delta H^o = -654.6\ kJ/mol \quad (3)$$

$$Sm_2O_2SO_{4(monocl)} \rightarrow Sm_2O_{3(cubic)} + SO_{2(gas)} + {}^1/_2O_{2(gas)};\ \Delta H^o = 170.8\ kJ/mol \quad (4)$$

140 Using the data on the enthalpies of samarium oxide [52] and sulfur oxide (IV) [53] formation, the
141 enthalpy of samarium oxysulfate formation was calculated by the Hess law and the value is equal to
142 $\Delta H^o_f(Sm_2O_2SO_{4\ (monocl)}) = -2294.0$ kJ/mol. Substituting the enthalpy of $Sm_2O_2SO_4$ formation in the
143 equation for calculating the enthalpy of reaction 4 and using the samarium oxysulfide formation
144 enthalpy $\Delta H^o_f(Sm_2O_2S_{(trig)}) = -1642.6$ kJ/mol [54], we obtain the theoretical samarium oxysulfide
145 oxidation enthalpy equal to –652.4 kJ/mol, which is perfectly compatible with the value determined
146 according to the DTA measurements.

147 To study the kinetics of the $Sm_2O_2SO_4$ formation and decomposition processes, the thermal
148 analysis of the samples was carried out at selected heating rates: 3, 5, 10, 15°C/min (Figure 1.b).
149 Based on the DTA data at the pointed heating rates, the process kinetic parameters were calculated.
150 The temperature dependence of the oxidation rate of Sm_2O_2S to $Sm_2O_2SO_4$ is characterized by
151 relatively moderate parameters for such processes: $E_a = 244$ kJ/mol, $A = 2 \cdot 10^{10}$. The activation energy
152 of the $Sm_2O_2SO_4$ decomposition to Sm_2O_3 is much higher and it is equal to 357 kJ/mol, but the
153 preexponential factor is an order of magnitude lower and is equal to $1 \cdot 10^9$. If we compare the
154 parameters with those known for $Eu_2O_2SO_4$ [14] (400 kJ/mol and $1 \cdot 10^{12}$, respectively), this
155 corresponds to wider peaks in the DTA curves for the $Eu_2O_2SO_4$ decomposition, which indicates its
156 higher kinetic stability, as compared to that of $Sm_2O_2SO_4$. In addition, the significantly higher
157 preexponential factor for the $Eu_2O_2SO_4$ decomposition, in comparison with that of $Sm_2O_2SO_4$,
158 suggests that the $Sm_2O_2SO_4$ symmetry is, at least, not higher than that of $Eu_2O_2SO_4$. The reduced
159 kinetic stability of $Sm_2O_2SO_4$, in comparison with that of $Eu_2O_2SO_4$, is in a good agreement with the
160 enthalpy values of compound decomposition.

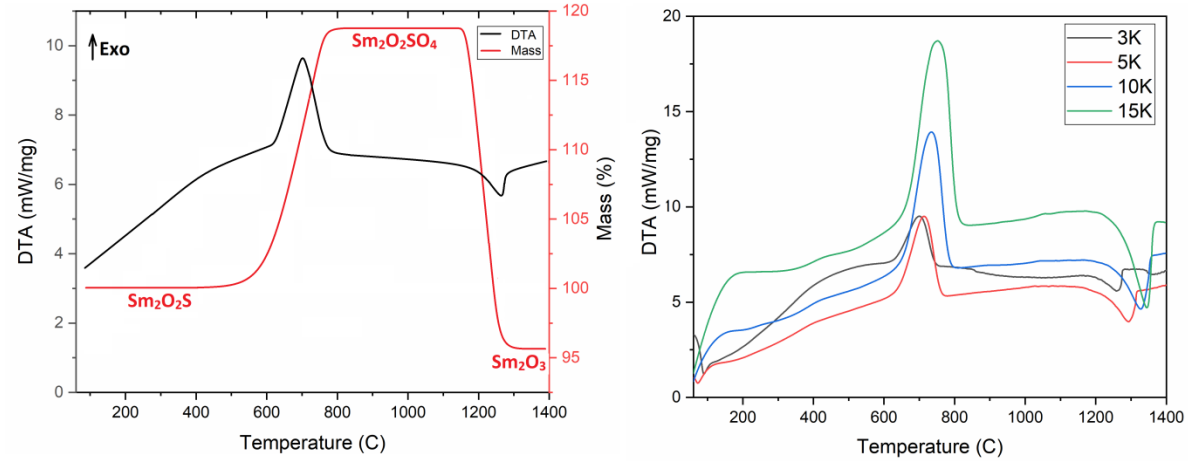

a) b)

161 **Figure. 1**.DTA/TG of Sm_2O_2S in synthetic air (a) and the shift of the peaks of thermal effects
162 depending on the heating rate (b).

163 *3.2. Isothermal oxidation of Sm_2O_2S*

164 At the temperature of 500ºC for 10 h, according to the results of X-ray phase analysis, there is no
165 phase composition change of the Sm_2O_2S sample (Figure 2.a). However, starting from 600°C, the
166 phase composition of the sample changes rapidly and, after only two hours, approximately a half of
167 Sm_2O_2S enters into the reaction (Figure 2.b). After five hours, only about 20% of samarium
168 oxysulfide remains in the sample (Figure 2.c). In 7 h of the process, the sample contains only pure

samarium oxysulfate (Figure 2.d). The temperature increase to 700°C leads to a sharp increase in the reaction rate and the complete oxidation of the sample is reached for 1 h. Such behavior differs significantly from the EuS oxidation process [35] where such pronounced rate temperature dependence is not observed. This effect is obviously related to the fact that only one reaction occurs during the Sm_2O_2S oxidation, in contrast to the EuS oxidation process, in which several parallel competing processes are realized. The samarium oxysulfide samples oxidation at 800, 900 and 1000ºC leads to the production of $Sm_2O_2SO_4$ samples for 1 h. An increase in the exposure time at these temperatures does not lead to a further change in the phase composition of the samples.

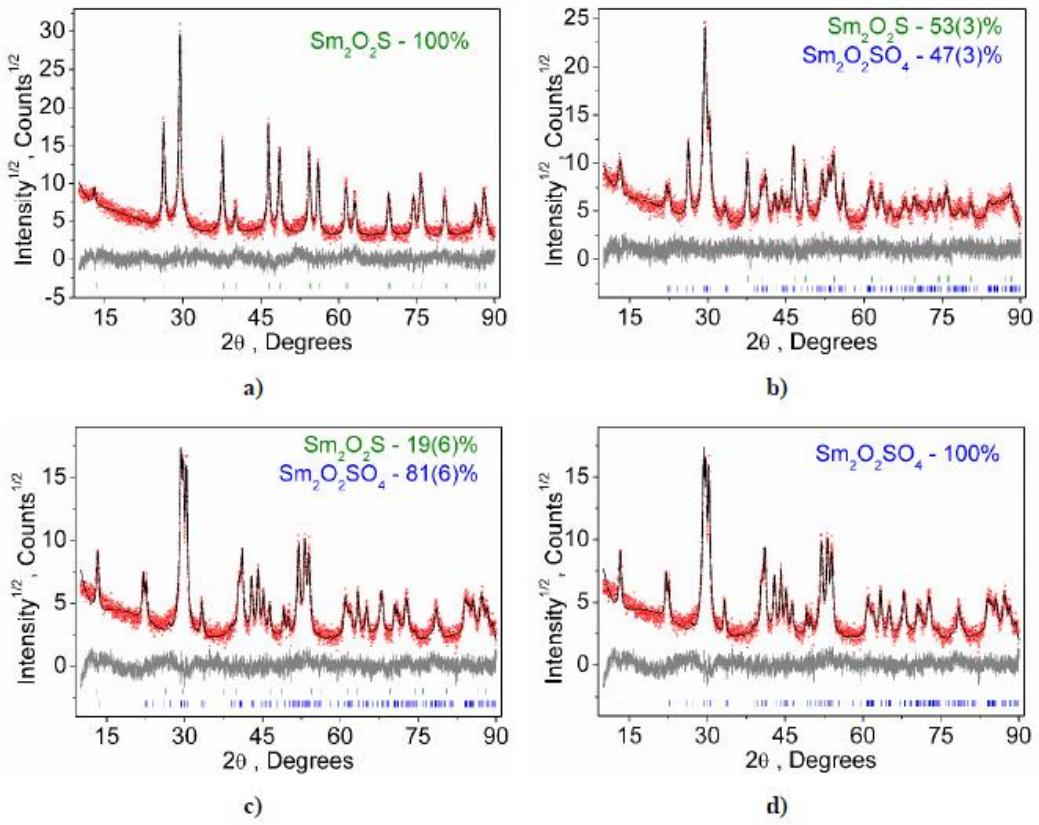

Figure 2.X-ray diffraction patterns of Sm_2O_2S (a) and the samples subjected to oxidation at 600ºC for 2 (b), 5 (c) and 7 h (d).

According to scanning electron microscopy, the samarium oxysulfide powder is formed by agglomerates sized 2-3 micrometers. The agglomerates have a clear granule structure. The initial granules have a size of about 50-100 nm (Figure 3.a). Carrying out the oxidation process at 600°C practically does not affect the change in the microstructure of the obtained $Sm_2O_2SO_4$ samples (Figure 3.b). A further increase in the process temperature leads to the agglomeration of the initial granules while maintaining the overall structure of the agglomerates (Figure 3.c, d). In the $Sm_2O_2SO_4$ sample obtained at 1000ºC, the initial granules have sizes from 250 nm to 0.5 μm. It should be pointed that the particle microstructure preservation is an important effect determining the possibility of applying the oxidation process to the synthesis of biocompatible materials based on rare earth oxysulfates [28-30].

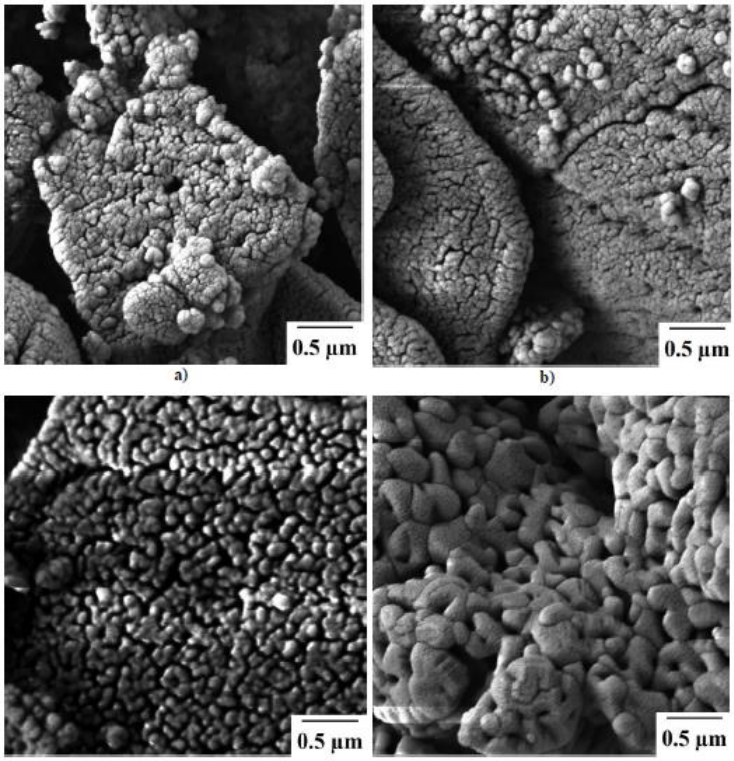

Figure 3.SEM images of Sm_2O_2S (a) and of $Sm_2O_2SO_4$ samples obtained at temperatures of 600 (b), 800 (c) and 1000ºC (d).

Based on the analysis of available experimental data on the phase composition of the samples obtained in isothermal processes, a kinetic diagram was built for the chemical composition changes during the samarium oxysulfide oxidation with air oxygen (Figure 4). In the diagram, three phase state fields can be observed. Two single-phase fields related to the stability conditions for compounds Sm_2O_2S (blue) and $Sm_2O_2SO_4$ (pink), and the intermediate two-phase field of Sm_2O_2S + $Sm_2O_2SO_4$ (orange), which boundaries are clearly governed by the thermodynamic and kinetic parameters of the process, are determined. As it is seen, the pure $Sm_2O_2SO_4$ phase can be synthesized at temperatures ≥700 °C for the reaction time 60-480 min. The phase field position in the diagram allows one to determine the conditions for the targeted preparation of the samples with specified phase compositions.

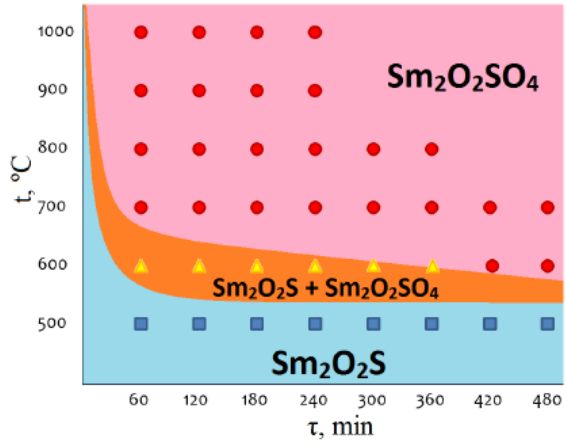

Figure 4. Kinetic scheme of changes in the chemical composition during the samarium oxysulfide oxidation.

3.3. Structural properties of $Sm_2O_2SO_4$

A sample of $Sm_2O_2SO_4$ for structural analysis was obtained by oxidizing samarium oxysulfide in air at 900ºC for 10 h. The Rietveld refinement was carried out by using TOPAS 4.2 [51] which accounts the esd's of each point by a special weight scheme. All peaks were indexed by a monoclinic cell (*C*2/*c*) with the parameters close to those of $Eu_2O_2SO_4$ [35] and, therefore, the crystal structure of $Eu_2O_2SO_4$ was taken as a starting model for Rietveld refinement. The Eu^{3+} site in the $Eu_2O_2SO_4$ structure was considered as occupied by the Sm^{3+} ion. In order to reduce the number of refined parameters, only one thermal parameter was refined for all O atoms. The refinement was stable and gave low *R*-factors (Table 1, Figure 5). The atom coordinates and main bond lengths obtained in $Sm_2O_2SO_4$ are summarized in Tables 2 and 3, respectively. The crystallographic data are deposited in the Cambridge Crystallographic Data Centre (CSD # 1968636). The data can be downloaded from the site (www.ccdc.cam.ac.uk/data_request/cif).

Table 1. Main parameters of processing and refinement of the $Sm_2O_2SO_4$sample.

Compound	**$Sm_2O_2SO_4$**
Sp.Gr.	*C*2/*c*
a, Å	13.7442 (2)
b, Å	4.20178 (4)
c, Å	8.16711 (8)
β, º	107.224 (1)
V, Å^3	450.498 (9)
Z	4
2*θ*-interval, º	10-140
R_{wp}, %	6.16
R_p, %	4.52
R_{exp}, %	2.78
χ^2	2.22
R_B, %	1.70

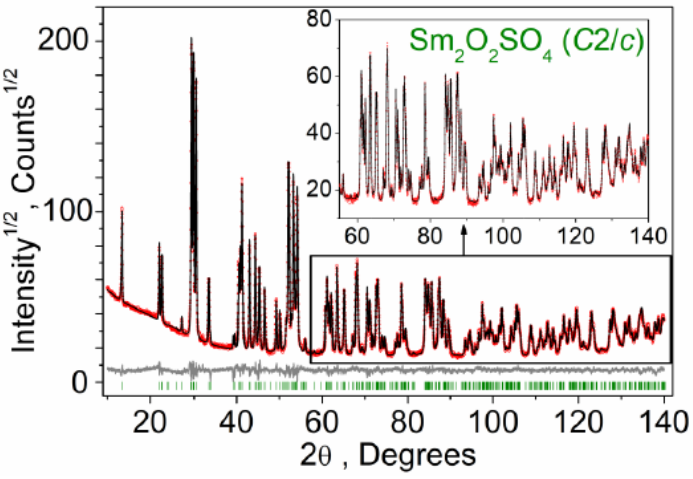

Figure 5. Difference Rietveld plot of $Sm_2O_2SO_4$.

Table 2. Fractional atomic coordinates and isotropic displacement parameters (Å^2) of $Sm_2O_2SO_4$.

	x	***y***	***z***	B_{iso}
Sm1	0.16930 (3)	0.5015 (4)	0.0850 (3)	0.45 (2)
S1	0	0.0339 (15)	0.25	1.63 (8)
O3	0.0904 (4)	0.8717 (12)	0.2840 (19)	0.75 (7)
O2	0.9996 (8)	0.2711 (12)	0.0985 (8)	0.75 (7)
O1	0.2474 (3)	0.022 (2)	0.120 (3)	0.75 (7)

Table 3. Main bond lengths (Å) of $Sm_2O_2SO_4$.

Sm1—O3	2.698 (9)	Sm1—O1^{v}	2.417 (10)
Sm1—O3^{i}	2.846 (13)	Sm1—O1^{vi}	2.291 (14)
Sm1-O3^{ii}	3.202 (3)	Sm1—O1^{vii}	2.346 (19)
Sm1—O2^{iii}	2.558 (9)	S1—O3^{viii}	1.372 (5)
Sm1—O2^{iv}	2.547 (8)	S1—O2^{iii}	1.588 (7)
Sm1—O1	2.259 (9)		

Symmetry codes: (i) *x*, -*y*+1, *z*-1/2; (ii) 1/2-x, -1/2+y, 1/2-*z*; (iii) *x*-1, *y*, *z*; (iv) -*x*+1, -*y*+1, -*z*; (v) *x*, *y*+1, *z*; (vi) -*x*+1/2, -*y*+1/2, -*z*; (vii) -*x*+1/2, *y*+1/2, -*z*+1/2; (viii) *x*, *y*-1, *z*.

The main difference of $Eu_2O_2SO_4$ and $Sm_2O_2SO_4$ structures is observed in their cell parameters and cell volumes. The former crystal has *a* = 13.65826(27), *b* = 4.188744(73), *c* = 8.14400(14) Å, β = 107.2819(21)°, *V* = 444.892(15) Å^3, and the compound under investigation $Sm_2O_2SO_4$ is characterized by *a* = 13.7442 (2), *b* = 4.20178 (4), *c* = 8.16711 (8) Å, β = 107.224 (1)°, *V* = 450.498 (9) Å^3. It is clearly seen that the cell parameters and cell volume of $Eu_2O_2SO_4$ are smaller than those of $Sm_2O_2SO_4$, and it is consistent with the fact that ion radius IR(Eu, CN=9) = 1.12 Å is smaller than IR(Sm, CN=9) = 1.132 Å.

As shown in Figure 6, the structure is represented by the alternation of cationic layers $[Sm_2O_2^{2+}]_n$ with the anionic layers consisting of isolated $[SO_4]^{2-}$tetrahedra. Both layers are parallel to (100) (Figure 6.a). All samarium atoms occupy identical crystallographic positions and are coordinated by nine oxygen atoms: five oxygen atoms belong to monodentate-bound sulfate groups, and the remaining oxygen atoms are bridging (Figure 6.c). Thus, the samarium atom in the structure forms a coordination environment shaped as a three-cap trigonal prism. Two caps of the coordination polyhedron, connected along the edge at the angle of 180°, form a plane of four oxygen atoms. The trigonal prism and caps in the coordination polyhedron are deformed due to the difference in the Sm-O bond lengths. One Sm-O

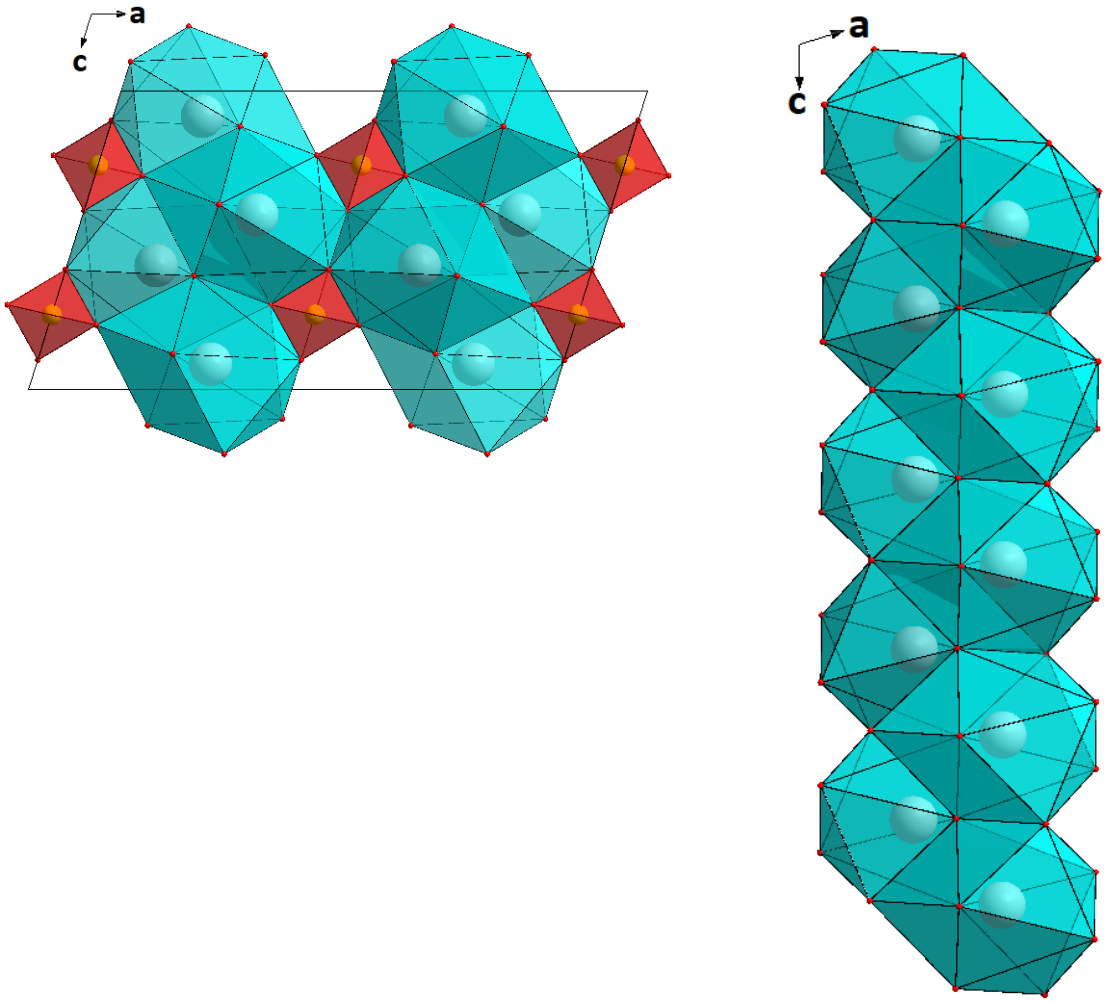

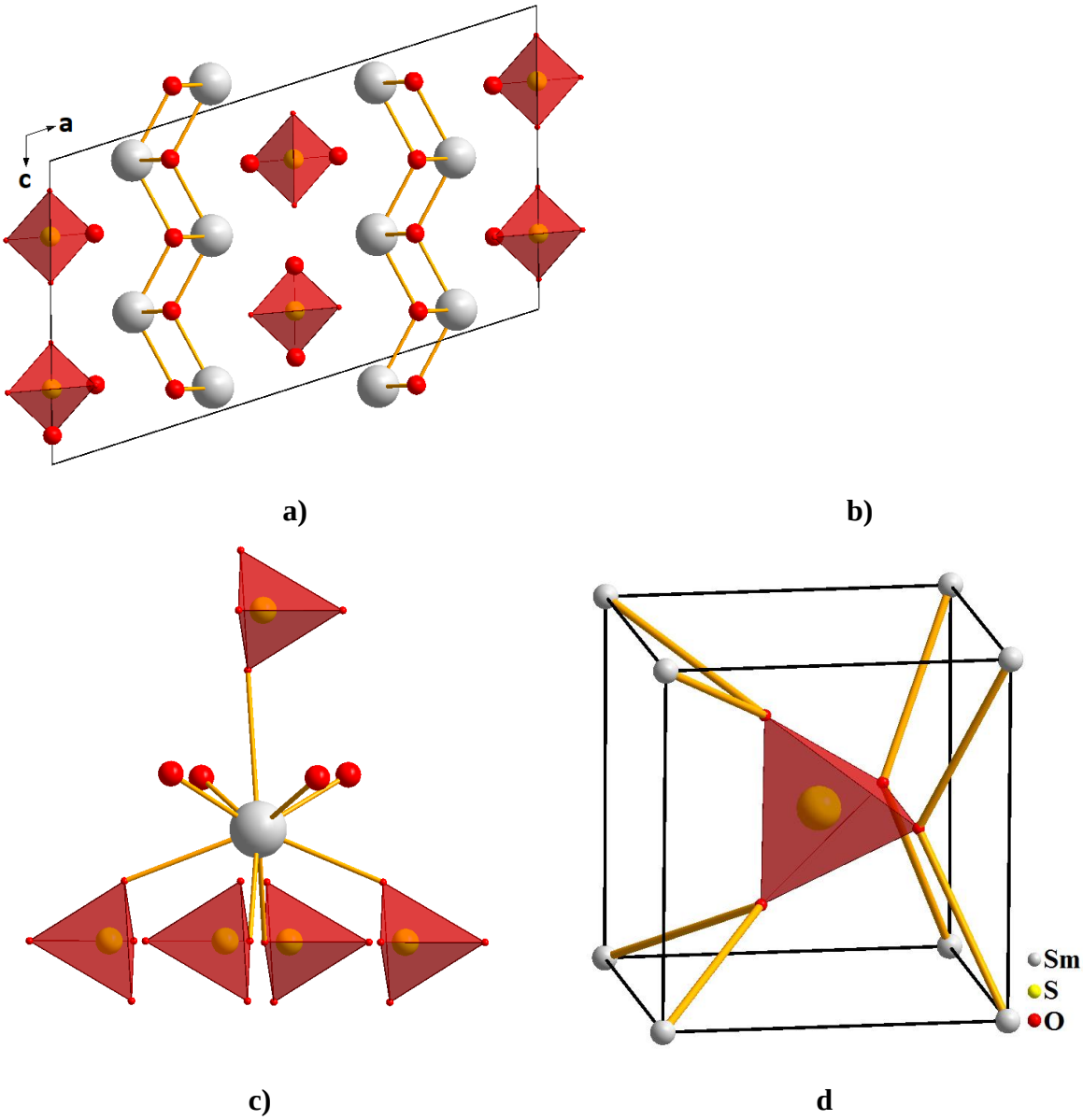

Figure 6. Projections of the $Sm_2O_2SO_4$ crystal structure (a), the structure of zigzag chains $[SmO_9]n$ (b), coordination of samarium (c) and coordination of sulfate tetrahedra (d) in the structure.

bond is much longer than the others. As a result, the coordination number of samarium is classified as 8 + 1. The SmO_9 polyhedra join with each other forming an infinite chain along the c-axis (Figure 6.b). The oxygen atoms of SO_4 groups are coordinated by sulfur and samarium atoms. The sulfate tetrahedron is surrounded by eight samarium atoms, resulting in the formation of a sphere-shaped coordination as almost a perfect cube (Fig. 6.d). Each bridging oxygen atom is coordinated by four samarium atoms, and it results in the formation of $[OSm_4]$ tetrahedra. These tetrahedra, sequentially pair wise connected with each other, form unlimited zigzag chains. The interconnected chains form unorganized layers (Figure 7).

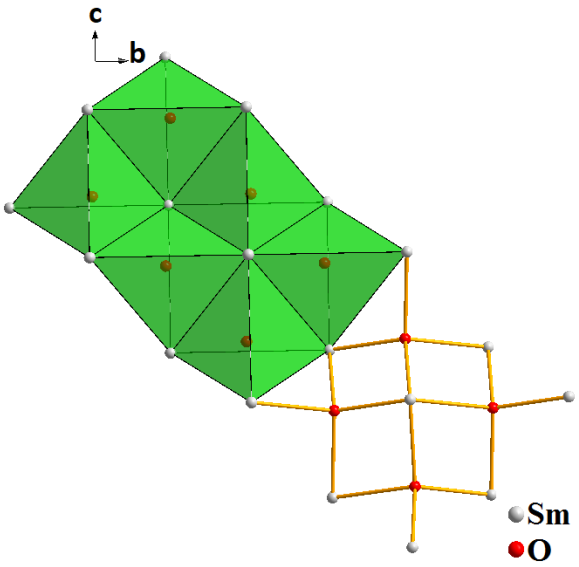

Figure 7. The cationic layers structure formed by the junction of tetrahedra [OSm_4].

3.4 Vibrational spectra of $Sm_2O_2SO_4$

Raman and Infrared spectra of $Sm_2O_2SO_4$ are shown in Figure 8. The vibrational irreducible representations for the monoclinic structure of $Sm_2O_2SO_4$ at the center of the Brillouin zone is Γ_{vibr} = $13A_g + 13A_u + 14B_g + 14B_u$, where $A_u + 2B_u$ are acoustic modes and $13A_g + 14B_g$ are Raman-active modes, while the $12A_u + 12B_u$ modes are active in IR spectra. The free tetrahedral $[SO_4]^{2-}$ ion of the T_d symmetry exhibits four internal vibrations. All four vibrations are Raman-active, whereas only ν_3 and ν_4 are Infrared-active. In the solid state, ν_3 and ν_4 may split into two or three bands because of the site effect [55]. The correlation diagram of internal vibrations between the free $[SO_4]^{2-}$ ions of the T_d symmetry, its site symmetry (C_2) and the factor group symmetry (C_{2h}) of a unit cell is given in Table 4.

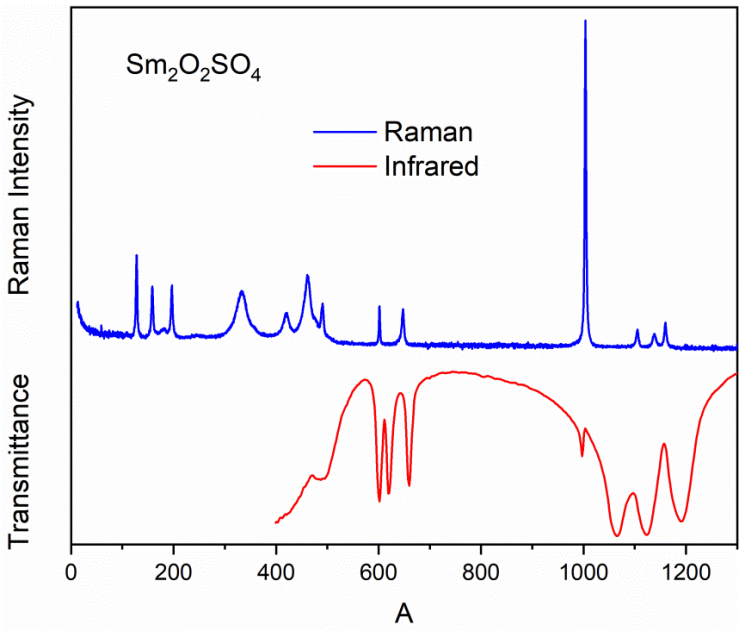

Figure 8. Raman and Infrared spectra of $Sm_2O_2SO_4$ powder.

Table 4. Correlation diagram of internal vibrations of the $[SO_4]^{2-}$ ions in the $Sm_2O_2SO_4$.

Wavenumber,cm^{-1}[55]	T_d Point group	C_2 Site symmetry	C_{2h} Factor group symmetry
983	A_1 (ν_1)	A	$A_g + A_u$
450	E(ν_2)	$2A$	$2A_g + 2A_u$
1105	E(ν_3)	$A + 2B$	$A_g + A_u + 2B_g + 2B_u$
611	E(ν_4)	$A + 2B$	$A_g + A_u + 2B_g + 2B_u$

From the correlation diagram, we can conclude that four spectral bands should be observed in the range of stretching vibrations of the SO_4 tetrahedra (975-1225 cm^{-1}) in Raman spectrum. The IR spectrum of the $Sm_2O_2SO_4$ structure should contain four bands in the range of stretching vibrations of $[SO_4]^{2-}$ ions, too. Three of them are ν_3 antisymmetric stretching and one is related to ν_1 symmetric stretching vibration. The ν_4 bending vibrations locate in the range of 575-675 cm^{-1}. The relevant spectral bands can be seen in Figures S2 and 8. The Raman bands associated with the ν_4 bending vibrations of SO_4 tetrahedra are overlapped with bands related to Sm-O vibrations, and these vibrations locate in the range of 300-500 cm^{-1}. The low-intensity bands in Raman spectra around 250 cm^{-1} should correspond to rotational vibrations of $[SO_4]^{2-}$ ions [56]. The remain spectral bands below 200 cm^{-1} are translational vibrations of SmO_9 polyhedra, SO_4 tetrahedra and Sm^{3+} ions.

3.5. Luminescent properties of $Sm_2O_2SO_4$

The $Sm_2O_2SO_4$ luminescence spectrum was recorded using the excitation by the GaN laser diode with the central wavelength 410 nm (24400 cm^{-1}) falling into three closely spaced Sm^{3+} transitions from the ground state $^6H_{5/2}$ to $^6P_{5/2}$, $^4M_{19/2}$ and $^4L_{13/2}$ excited states. The obtained spectrum is presented in Figure 9 in comparison with the luminescence spectrum of another highly concentrated samarium-containing $BaSm_2(MoO_4)_4$ crystal [39]. The structure of luminescence spectra of both $Sm_2O_2SO_4$ and the reference crystal is rather similar and exhibits three main bands easily assignable to the transitions from the $^4G_{5/2}$ state to $^6H_{5/2}$, $^6H_{7/2}$, and $^6H_{9/2}$ multiplets. However, the distribution of the intensities between three mentioned channels in $Sm_2O_2SO_4$ is slightly different from that of the reference crystal, while the red transition to the $^6H_{9/2}$ state dominates in the reference crystal, the orange transition to the $^6H_{7/2}$ state prevails in $Sm_2O_2SO_4$. This difference demonstrates the possibility of controlling the samarium ion emission chromaticity via the crystal field engineering that allows certain variation of Judd-Ofelt intensity parameters. We must note that the reference crystal spectrum was divided by 10 for a better comparison of the shapes. Therefore, we must deduce that concentration quenching of the luminescence in $Sm_2O_2SO_4$ is rather high in comparison with, e.g., molybdate crystalline lattices.

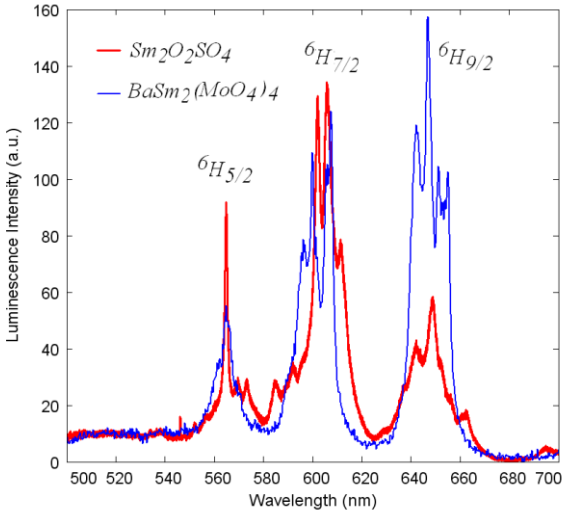

Figure 9. The luminescence spectra of $Sm_2O_2SO_4$ (red) and of the reference crystal ($BaSm_2(MoO_4)_4$, blue). For better comparison, the reference crystal spectrum is divided by 10.

4. Conclusions

Thus, a comprehensive study of the samarium oxysulfide oxidation process was carried out. The kinetic and thermodynamic characteristics of the process were established. The effect of oxidation temperature on the morphology of samarium oxysulfate samples was evaluated. The main structural and spectroscopic characteristics of samarium oxysulfate were determined. According to the X-ray powder diffraction data, the monoclinic symmetry was established. The main structural elements and their influence on the properties of the compound were analyzed. The theoretical calculations of vibration spectra confirm the adequacy of the structural model, which is important for such complex structures with the ambiguity in the choice of the structural model. The $Sm_2O_2SO_4$ luminescent-spectral characteristics were determined. The luminescence spectrum consists of three main luminescent bands originating from the $^4G_{5/2}$ state, the transition to $^6H_{7/2}$ in the orange part of the spectrum being dominant.

Acknowledgments: This work was partially supported by the Russian Foundation for Basic Research (Grant 18-02-00754). A.S. Aleksandrovsky, A.S. Krylov and A.S. Oreshonkov are grateful to the Basic Project of the Ministry of Science of the Russian Federation. Also, this work was partly supported by the Russian Science Foundation (project 19-42-02003, in the part of conceptualization). Use of equipment of Krasnoyarsk Regional Center of Research Equipment of Federal Research Center «Krasnoyarsk Science Center SB RAS» is acknowledged.

Conflicts of Interest: Declare conflicts of interest or state "The authors declare no conflict of interest." Authors must identify and declare any personal circumstances or interest that may be perceived as inappropriately influencing the representation or interpretation of reported research results. Any role of the funders in the design of the study; in the collection, analyses or interpretation of data; in the writing of the manuscript, or in the decision to publish the results must be declared in this section. If there is no role, please state "The funders had no role in the design of the study; in the collection, analyses, or interpretation of data; in the writing of the manuscript, or in the decision to publish the results".

References

1. P. O. Andreev, E. I. Sal'nikova, A. A. Kislitsyn, Kinetics of the transformation of $Ln_2O_2SO_4$ into Ln_2O_2S (Ln = La, Pr, Nd, and Sm) in a hydrogen flow, Russ. J. Phys. Chem. A**2013**, 87, 1482–1487.
2. E. I. Sal'nikova, P. O. Andreev, S. M. Antonov, Kinetic diagrams of $Ln_2O_2SO_4$ phase transformations in a H_2 flow (Ln = La, Pr, Nd, Sm), Russ. J. Phys. Chem. A **2013**, 87, 1280–1283.
3. E. I. Sal'nikova, D. I. Kaliev, P. O. Andreev, Kinetics of phase formation upon the treatment of $La_2(SO_4)_3$ and $La_2O_2SO_4$ in a hydrogen flow, Russ. J. Phys. Chem. A **2011**, 85, 2121–2125.
4. L. C. Machado, M. T. D. de Azeredo, H. P. S. Corrêa, J. do Rosário Matos, Í. O. Mazali, Formation of oxysulfide LnO_2S_2 and oxysulfate LnO_2SO_4 phases in the thermal decomposition process of lanthanide sulfonates (Ln = La, Sm), J. Therm. Anal. Calorim.**2012**, 107, 305–311.
5. S. Kim, T. Masui, N. Imanaka, Synthesis of red-emitting phosphors based on gadolinium oxysulfate by a flux method, Electrochemistry **2009**, 77, 611–613.
6. T. Kijima, T. Shinbori, M. Sekita, M. Uota, G. Sakai, Abnormally enhanced Eu^{3+} emission in $Y_2O_2SO_4$:Eu^{3+} inherited from their precursory dodecylsulfate-templated concentric-layered nanostructure, J. Lumin. **2008**, 128, 311–316.
7. T. Kijima, T. Isayama, M. Sekita, M. Uota, G. Sakai, Emission properties of Tb^{3+} in $Y_2O_2SO_4$ derived from their precursory dodecylsulfate-templated concentric- and straight-layered nanostructures, J. Alloys Compd. **2009**, 485, 730–733.
8. M. Machida, K. Kawamura, K. Ito, K. Ikeue, Large-capacity oxygen storage by lanthanide oxysulfate/oxysulfide systems, Chem. Mater. **2005**, 17, 1487–1492.
9. M. Machida, K. Kawamura, T. Kawano, D. Zhang, K. Ikeue, Layered Pr-dodecyl sulfate mesophases as precursors of $Pr_2O_2SO_4$ having a large oxygen-storage capacity, J. Mater. Chem. **2006**, 16, 3084.

10. M. Machida, T. Kawano, M. Eto, D. Zhang, K. Ikeue, Ln dependence of the large-capacity oxygen storage/release property of Ln oxysulfate/oxysulfide systems, Chem. Mater. **2007**, 19, 954–960.
11. D. Zhang, F. Yoshioka, K. Ikeue, M. Machida, synthesis and oxygen release/storage properties of Ce-substituted La-oxysulfates, $(La_{1-x}Ce_x)_2O_2SO_4$, Chem. Mater. **2008**, 20, 6697–6703.
12. Y. G. Denisenko, A. S. Aleksandrovsky, V. V. Atuchin, A. S. Krylov, M. S. Molokeev, A. S. Oreshonkov, N. P. Shestakov, O. V. Andreev, Exploration of structural, thermal and spectroscopic properties of self-activated sulfate $Eu_2(SO_4)_3$ with isolated SO_4 groups, J. Ind. Eng. Chem. **2018**, 68, 109–116.
13. I. Hartenbach, Th. Schleid, Serendipitous Formation of Single-Crystalline $Eu_2O_2[SO_4]$, Z. Anorg. Allg. Chem. **2002**, 628, 2172.
14. Y. G. Denisenko, N. A. Khritokhin, O. V. Andreev, S. A. Basova, E. I. Sal'nikova, A. A. Polkovnikov, Thermal decomposition of europium sulfates $Eu_2(SO_4)_3{\cdot}8H_2O$ and $EuSO_4$, J. Solid State Chem. **2017**, 255, 219–224.
15. J. A. Poston, R. V. Siriwardane, E. P. Fisher, A. L. Miltz, Thermal decomposition of the rare earth sulfates of cerium (III), cerium (IV), lanthanum (III) and samarium (III), Appl. Surf. Sci. **2003**, 214, 83–102.
16. J. Liang, R. Ma, F. Geng, Y. Ebina, T. Sasaki, $Ln_2(OH)_4SO_4{\cdot}nH_2O$ (Ln = Pr to Tb; n ~ 2): a new family of layered rare-earth hydroxides rigidly pillared by sulfate ions, Chem. Mater. **2010**, 22, 6001–6007.
17. F. Chen, G. Chen, T. Liu, N. Zhang, X. Liu, H. Luo, J. Li, L. Chen, R. Ma, G. Qiu, Controllable fabrication and optical properties of uniform gadolinium oxysulfate hollow spheres, Sci. Rep. **2016**, 5, 17934.
18. D. Zhang, T. Kawada, F. Yoshioka, M. Machida, Oxygen gateway effect of $CeO_2/La_2O_2SO_4$ composite oxygen storage materials, ACS Omega **2016**, 1, 789–798.
19. T. H. Xing, L. X. Song, J. Xiong, H. B. Cao, P. F. Du, Preparation and luminescent properties of Tb^{3+} doped $Y_2O_2SO_4$microflakes, Adv. Appl. Ceram.**2013**, 112, 455–459.
20. E. I. Sal'nikova, Y. G.Denisenko, A. S. Aleksandrovsky, I. E. Kolesnikov, E. Lähderanta, P. O. Andreev, N. O. Azarapin, O. V. Andreev, S. A. Basova, A. V. Matigorov, Synthesis and optical properties RE_2O_2S: Ln (RE= La, Y; Ln= Ce, Eu, Dy, Er), J. Solid State Chem. **2019**, 279, 120964.
21. M. Gaft, Y. Raichlin, F. Pelascini, G. Panzer, V. Motto Ros, Imaging rare-earth elements in minerals by laser-induced plasma spectroscopy: Molecular emission and plasma-induced luminescence, Spectrochim. Acta Part B At. Spectrosc. **2019**, 151, 12–19.
22. M. Yu, H. Xu, Y. Li, Q. Dai, G. Wang, W. Qin, Morphology luminescence and photovoltaic performance of lanthanide-doped $CaWO_4$ nanocrystals, J. Colloid Interface Sci. **2020**, 559, 162–168.
23. J. Zhang, G. Chen, Z. Zhai, H. Chen, Y. Zhang, Optical temperature sensing using upconversion luminescence in rare-earth ions doped $Ca_2Gd_8(SiO_4)_6O_2$ phosphors, J. Alloys Compd. **2019**, 771, 838–846.
24. J. Pejchal, J. Barta, T. Trojek, R. Kucerkova, A. Beitlerova, M. Nikl, Luminescence and scintillation properties of rare-earth-doped $LaAlO_3$ single crystals, Radiat. Meas. **2019**, 121, 26–31.
25. S. E. Kichanov, Y. E. Gorshkova, G. E. Rachkovskaya, D. P. Kozlenko, G. B. Zakharevich, B. N. Savenko, Structural evolution of luminescence nanoparticles with rare-earth ions in the oxyfluoride glass ceramics, Mater. Chem. Phys. **2019**, 237, 121830.
26. V. V. Atuchin, A. S. Aleksandrovsky, O. D. Chimitova, T. A. Gavrilova, A. S. Krylov, M. S. Molokeev, A. S. Oreshonkov, B. G. Bazarov, J. G. Bazarova, Synthesis and spectroscopic properties of monoclinic α-$Eu_2(MoO_4)_3$, J. Phys. Chem. C **2014**, 118, 15404–15411.
27. C.S. Lim, V.V. Atuchin, A.S. Aleksandrovsky, Yu.G. Denisenko, M.S. Molokeev, A.S. Oreshonkov, Fabrication of microcrystalline $NaPbLa(WO_4)_3$:Yb^{3+}/Ho^{3+} phosphors and their upconversion photoluminescent characteristics. Korean J. Mater. Res. **2019**, 29, 741-746.
28. S. A. Osseni, Y. G. Denisenko, J. K. Fatombi, E. I. Sal'nikova, O. V Andreev, Synthesis and characterization of $Ln_2O_2SO_4$ (Ln = Gd, Ho, Dy and Lu) nanoparticles obtained by coprecipitation method and study of their reduction reaction under H_2 flow, J. Nanostructure Chem. **2017**, 7, 337–343.
29. S. A. Osseni, S. Lechevallier, M. Verelst, C. Dujardin, J. Dexpert-Ghys, D. Neumeyer, M. Leclercq, H. Baaziz, D. Cussac, V. Santran, R. Mauricot, New nanoplatform based on Gd_2O_2S:Eu^{3+} core: synthesis, characterization and use for in vitro bio-labelling, J. Mater. Chem. **2011**, 21, 18365.
30. S. A. Osseni, S. Lechevallier, M. Verelst, P. Perriat, J. Dexpert-Ghys, D. Neumeyer, R. Garcia, F. Mayer, K. Djanashvili, J. A. Peters, et al., Gadolinium oxysulfide nanoparticles as multimodal imaging agents for T_2-weighted MR, X-ray tomography and photoluminescence, Nanoscale **2014**, 6, 555–564.

31. A. E. Sedykh, D. G. Kurth, K. Müller-Buschbaum, Two series of lanthanide coordination polymers and complexes with 4′-phenylterpyridine and their luminescence properties, Eur. J. Inorg. Chem. **2019**, 4564–4571.
32. T. Ribbeck, C. Kerpen, D. Löw, A. E. Sedykh, K. Müller-Buschbaum, N. V. Ignat'ev, M. Finze, Lanthanide trifluoromethyltricyanoborates: Synthesis, crystal structures and thermal properties, J. Fluor. Chem. 2019, 219, 70–78.
33. J. M. Stangl, D. Dietrich, A. E. Sedykh, C. Janiak, K. Müller-Buschbaum, Luminescent MOF polymer mixed matrix membranes for humidity sensing in real status analysis, J. Mater. Chem. C **2018**, 6, 9248–9257.
34. V. V. Atuchin, A. S. Aleksandrovsky, B. G. Bazarov, J. G. Bazarova, O. D. Chimitova, Y. G. Denisenko, T. A. Gavrilova, A. S. Krylov, E. A. Maximovskiy, M. S. Molokeev, et al., Exploration of structural, vibrational and spectroscopic properties of self-activated orthorhombic double molybdate $RbEu(MoO_4)_2$ with isolated MoO_4 units, J. Alloys Compd. **2019**, 785, 692–697.
35. Y. G. Denisenko, M. S. Molokeev, A. S. Krylov, A. S. Aleksandrovsky, A. S. Oreshonkov, V. V. Atuchin, N. O. Azarapin, P. E. Plyusnin, E. I. Sal'nikova, O. V. Andreev, High-Temperature Oxidation of Europium (II) Sulfide, J. Ind. Eng. Chem. **2019**, 79, 62–70.
36. O. V. Andrrev, I. A. Razumkova, A. N. Boiko, Synthesis and thermal stability of rare earth compounds REF_3, $REF_3{\cdot}nH_2O$ and $(H_3O)RE_3F_{10}{\cdot}nH_2O$ (RE= Tb−Lu, Y), obtained from sulphide precursors, J. Fluor. Chem. **2018**, 207, 77–83.
37. I. A. Razumkova, A. N. Boiko, O. V. Andreev, S. A. Basova, Synthesis of $[(H_3O)Tm_3F_{10}] \cdot nH_2O$, ErF_3, and TmF_3 powders and their physicochemical properties, Russ. J. Inorg. Chem. **2017**, 62, 418–422.
38. I. A. Razumkova, Synthesis of $NaYF_4$ compounds from sulfide precursors, J. Fluor. Chem. **2018**, 205, 1–4.
39. V. V. Atuchin, A. S. Aleksandrovsky, M. S. Molokeev, A. S. Krylov, A. S. Oreshonkov, D. Zhou, Structural and spectroscopic properties of self-activated monoclinic molybdate $BaSm_2(MoO_4)_4$, J. Alloys Compd. **2017**, 729, 843–849.
40. V. V. Atuchin, A. S. Aleksandrovsky, O. D. Chimitova, C.-P. Diao, T. A. Gavrilova, V. G. Kesler, M. S. Molokeev, A. S. Krylov, B. G. Bazarov, J. G. Bazarova, et al., Electronic structure of β-$RbSm(MoO_4)_2$ and chemical bonding in molybdates, Dalt. Trans. **2015**, 44, 1805–1815.
41. V. V. Atuchin, A. K. Subanakov, A. S. Aleksandrovsky, B. G. Bazarov, J. G. Bazarova, T. A. Gavrilova, A. S. Krylov, M. S. Molokeev, A. S. Oreshonkov, S. Y. Stefanovich, Structural and spectroscopic properties of new noncentrosymmetric self-activated borate $Rb_3EuB_6O_{12}$ with B_5O_{10} units, Mater. Des. **2018**, 140, 488–494.
42. H. Ji, Z. Huang, Z. Xia, M. S. Molokeev, X. Jiang, Z. Lin, V. V. Atuchin, Comparative investigations of the crystal structure and photoluminescence property of eulytite-type $Ba_3Eu(PO_4)_3$ and $Sr_3Eu(PO_4)_3$, Dalt. Trans. **2015**, 44, 7679–7686.
43. V. Biondo, P. W. C. Sarvezuk, F. F. Ivashita, K. L. Silva, A. Paesano, O. Isnard, Geometric magnetic frustration in RE_2O_2S oxysulfides (RE= Sm, Eu and Gd), Mater. Res. Bull. **2014**, 54, 41–47.
44. C. Yu, M. Yu, C. Li, X. Liu, J. Yang, P. Yang, J. Lin, Facile sonochemical synthesis and photoluminescent properties of lanthanide orthophosphate nanoparticles, J. Solid State Chem. **2009**, 182, 339–347.
45. C. Cascales, B. G. Lor, E. G. Puebla, M. Iglesias, M. A. Monge, C. R. Valero, N. Snejko, Catalytic behavior of rare-earth sulfates: Applications in organic hydrogenation and oxidation reactions, Chem. Mater. **2004**, 16, 4144–4149.
46. Z. Xu, C. Li, Z. Hou, C. Peng, J. Lin, Morphological control and luminescence properties of lanthanide orthovanadate $LnVO_4$ (Ln= La to Lu) nano-/microcrystals via hydrothermal process, CrystEngComm**2011**, 13, 474–482.
47. R. L. Blaine, H. E. Kissinger, Homer Kissinger and the Kissinger equation, Thermochim. Acta, **2012**, 540, 1–6.
48. N. Bukovec, P. Bukovec, J. Šiftar, Kinetics of the thermal decomposition of $Pr_2(SO_4)_3$ to $Pr_2O_2SO_4$, Thermochim. Acta, **1980**, 35, 85–91.
49. A. S. Lyadov, V. V. Kurilkin, Reduction specifics of rare-earth orthovanadates (REE= La, Nd, Sm, Dy, Ho, Er, Tm, Yb, and Lu), Russ. J. Inorg. Chem. **2016**, 61, 86-92.
50. J. Llópiz, M. M. Romero, A. Jerez, Y. Laureiro, Kinetic analysis of thermogravimetric data, Thermochim. Acta 1995, 256, 205–211.
51. Bruker AXS TOPAS V4: User's Manual. Bruker AXS, Karlsruhe, Germany.**2008**.

52. F. B. Baker, G. C. Fitzgibbon, D. Pavone, C. E. Holley, L. D. Hansen, E. A. Lewis, Enthalpies of formation of Sm_2O_3 (monoclinic) and Sm_2O_3 (cubic), J. Chem. Thermodyn. **1972**, 4, 621–636.
53. J. R. Eckman, F. D. Rossini, Bur. Stand. J. Res. **1929**, 3, 597.
54. Y. L. Suponitskiy, Thesis of Doctor of Science in Chemistry, D. Mendeleev University of Chemical Technology of Russia, Moscow. **2002**.
55. K. Nakamoto, Infrared and Raman Spectra of Inorganic and Coordination Compounds, 6th edn.Wiley, New York etc., **2009**.
56. Y.G. Denisenko, V.V. Atuchin, M.S. Molokeev, A.S. Aleksandrovsky, A.S. Krylov, A.S. Oreshonkov, S.S. Volkova and O.V. Andreev,Structure, thermal stability, and spectroscopic properties of triclinic double sulfate $AgEu(SO_4)_2$ with isolated SO_4groups, Inorg. Chem. **2018**, 57, 13279−13288.

Sample Availability: Samples of the compounds ..... are available from the authors.